Modeling and Control of the WPT System Subject to Input Nonlinearity and Communication Delay

Shijun Zhao, Chunsen Tang, *Member, IEEE*, Fengwei Chen, Dan Zhao, Pengqi Deng, and Jing Xiao

***Abstract*—Wireless power transfer (WPT) systems are a kind of high-order, highly nonlinear, time-delay systems. The conventional circuit theory-based methods for modeling the system result in high-order models, so it may not be efficient in digital implementation, especially on cost-sensitive microcontrollers. Besides, the time delay will impair the feedback performance of the system, and even lead to closed-loop instability under incorrectly compensated. To solve the abovementioned problems, this article proposes to infer a low-order model for the system based on sampled data and then use this model to design the control system. More precisely, the proposed methodology consists of two steps. In the first step, a parsimonious modeling method is proposed to yield a low-order model of Hammerstein type plus time delay, which makes it possible to simulate the model response in a cost-sensitive microcontroller. Then, based on the model obtained in the previous step, the internal model control (IMC) is adopted to design the closed-loop control system. Benefiting from the accurate prediction provided by the model, the closed-loop controller can mitigate the effect of the time delay and track the set value quickly. Finally, experimental and comparative results are given to verify the effectiveness of the proposed method.**

***Index Terms*—Data-driven modeling, Hammerstein model, internal model control (IMC), nonlinear system, time delay, wireless power transfer (WPT).**

I. Introduction

WIRELESS power transfer (WPT) systems have attracted considerable attention due to their abilities to obtain electrical energy without physical contact, thereby improving the safety, reliability, and flexibility of the power supply [1], [2], [3]. These advantages have made it widely applicable in many fields, especially in electric vehicles, oil drilling, biomedical, aviation, and marine industries [4], [5], [6], [7], [8], [9], [10].

In most WPT systems, a closed-loop control is necessary to ensure the stability of the system output voltage and the safety of power devices [11], [12]. Since an accurate model can help in controller design so as to improve the control system performance, it is necessary to obtain a model that accurately describe the input and output behavior of the system. Conventional modeling methods for the WPT system include generalized state-space averaging (GSSA) [13], expansion function description [14], discrete time mapping [15], ac impedance analysis [16], etc. It should be noted that the abovementioned methods concentrate on circuit-level modeling, and most of these yield steady-state models, while the system-level model (dynamic modeling), which is helpful for control system design, has been considered less important. Due to the high nonlinearity of the WPT system, the process of traditional modeling method is usually complex, including high-order modeling and model reduction [15], [17]. Then, the uncertainty of various circuit topologies, system parameters, operating states, and control methods can result in the traditional model obtained by traditional methods being unable to reflect the real system in specific scenarios. Besides, the WPT system forms a closed loop through the communication link between the primary side and the secondary side, as shown in Fig. 1, where the wireless communication, data sampling, processor calculation and model reduction in the system will lead to a time delay [18]. The time delay may lead to instability of the system and failure of the closed-loop system if it has not been accurately handled. Due to the high-order models, and that time delays cannot be accurately estimated by traditional modeling methods, it is necessary to find a new method that is able to yield a simple model with a time delay for the WPT system and, on this basis, design

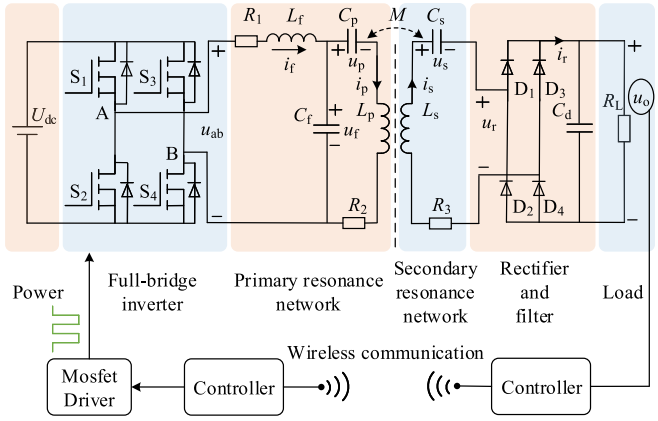

Fig. 1. Architecture of the wireless power transfer system under consideration.

Manuscript received 15 March 2023; revised 12 June 2023; accepted 18 August 2023. Date of publication 23 August 2023; date of current version 22 September 2023. This work was supported by the National Natural Science Foundation of China under Grants 52277002 and 62073246. Recommended for publication by Associate Editor J.-i. (GAE) Itoh. *(Corresponding author: Chunsen Tang.)*

Shijun Zhao, Chunsen Tang, Fengwei Chen, Dan Zhao, and Pengqi Deng are with the School of Automation, Chongqing University, Chongqing 400044, China (e-mail: zsjwpt@cqu.edu.cn; cstang@cqu.edu.cn; fengwei.chen@cqu.edu.cn; dan.zhao@stu.cqu.edu.cn; 357619947@qq.com).

Jing Xiao is with the Southern Power Grid Corporation Wireless Power Transmission Joint Laboratory Guangxi Power Grid Company, Ltd, Nanning 530023, China (e-mail: 442756088@qq.com).

Color versions of one or more figures in this article are available at https://doi.org/10.1109/TPEL.2023.3307691.

Digital Object Identifier 10.1109/TPEL.2023.3307691

a controller with delay compensation to further improve the control performance.

A Hammerstein model is composed of a static nonlinear function and a linear time-invariant model, which has been used to describe a buck converter [19], an insulated gate bipolar transistor (IGBT) [20], and a dc/dc converter [21]. It represents a direct way to incorporate prior information about static nonlinearity into the converter model and can better describe the nonlinear system model [22]. The Hammerstein model can be identified via data-driven modeling, which has been widely used in industry. With this method, the structure, parameters, and time delay of the model are determined from sampled input and output data according to the specified performance indicators, rather than the circuit topology and parameters [23], [24]. The sampled input and output data required for model identification are very easy to obtain. These show that data-driven modeling is superior to the traditional modeling method from a control perspective, and has attracted more and more attention in the field of power electronics [25], [26].

The feedback control of the WPT system is subject to parameter uncertainty, nonlinearity, time delay, etc. In these circumstances, the traditional proportional-integral-derivative (PID) control is insufficient to achieve satisfactory control performance. At the same time, the tuning of controller parameters often depends on engineering experience, and the process of parameter tuning is nontrivial. For a time-delay process, in order to ensure the closed-loop stability using a PID controller, it is necessary to reduce the integral effect, which will slow down the closed-loop response and degrade the control quality [27], [28]. The internal model control (IMC) is simple to design and it can greatly improve the robustness and disturbance rejection performance of the system, especially in large time-delay systems [29], [30], [31], which motivates its research to address the above problems in the WPT system. In our previous research works, the data-driven modeling of SISO and MISO WPT systems, using continuous-time or discrete-time transfer function models with time delays to explain the behavior of input–output systems, has been investigated. The method is based on the refined instrumental variable (RIV) to estimate the model parameters and time delay at a static operation point, and it shows that a first- or second-order model can explain very well the input–output behavior of a system [23], [24], [32]. Due to the nonlinear characteristics of the WPT system, the model parameters at the different static points can be different. In this case, a Hammerstein model could be a better choice to take the nonlinearities into account. Therefore, our previous research will be improved and extended in this article to estimate the Hammerstein model. On this basis, IMC is designed to improve the control quality in the presence of time delays and nonlinearity. The contributions of this article are as follows.

1) The Hammerstein model is used to describe the *LCC*-S compensated WPT system, and the method of data-driven modeling is applied to simultaneously estimate system parameters and time delay of a Hammerstein model.
2) Based on the identified Hammerstein model, the IMC method is adopted to improve the control quality considering input nonlinearities and communication time delays.

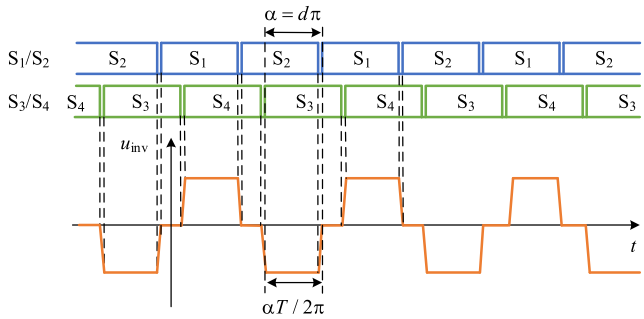

Fig. 2. Example of the PS control and inverter output voltage.

The rest of this article is organized as follows. In Section II, the Hammerstein model is established to describe the nonlinear behavior of the *LCC*-S WPT system, and a data-driven modeling method is proposed to estimate the parameters of this model. In Section III, the Hammerstein-model-based IMC design method is introduced. Simulation and experimental results are shown in Section IV to demonstrate the effectiveness of the proposed method. Finally, Section V concludes this article.

II. System Structure and Modeling Method

A. System Description

As shown in Fig. 1, the commonly used *LCC*-S WPT system is studied. The *LCC* composite compensation mode on the primary side is adopted, while the *LC* series compensation mode on the secondary side is adopted. u_{ab} represents the first harmonic of the inverter output voltage. R_1, R_2, and R_3 represent the resistances of the compensation inductor L_{f}, transmitter coil L_{p}, and receiver coil L_{s}, respectively. M represents the mutual induction between the transmitting coil and the receiving coil. R_{L} denotes the equivalent load of user equipment. f_0 denotes the operating frequency of the system. Generally, the output voltage is fed back to the primary side through wireless communication, and then the controller adjusts the phase shifting of the inverter to regulate the output voltage. The signals in phase-shift (PS) control of the inverter are shown in Fig. 2, where d represents the duty cycle of the PS angle. α represents the angle at duration which switches S_1 and S_4 (or S_2 and S_3) are opened at the same time. Through the error between the output voltage and the set value, the duty cycle d is calculated. The previous studies have shown the nonlinearity of the system in Fig. 1 [33]; see Fig. 3, where the output characteristic curve of the system described in Fig. 1 at different duty cycles is shown. In Fig. 3(a), the steady-state output voltages of the system under different duty cycle differs from each other: they increase with the increase of the duty cycle along a nonlinear trajectory. In Fig. 3(b), the step responses of the system at the different steady-state operating points are shown, where a small duty cycle disturbance is superimposed on the input. The response trend is similar at different steady-state operating points, except for the gain. Inspired by this, it is reasonable to describe the WPT system by a Hammerstein model [34]. In the rest of the article, the modeling process will be introduced and analyzed in detail.

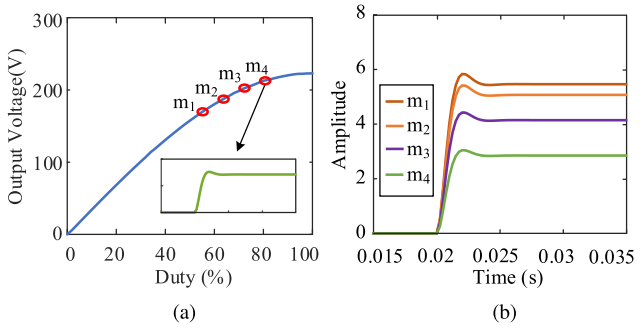

Fig. 3. Static nonlinearity. (a) Steady-state outputs as a function of duty cycle. (b) Output responses to a 2% increment in duty cycle at different static points.

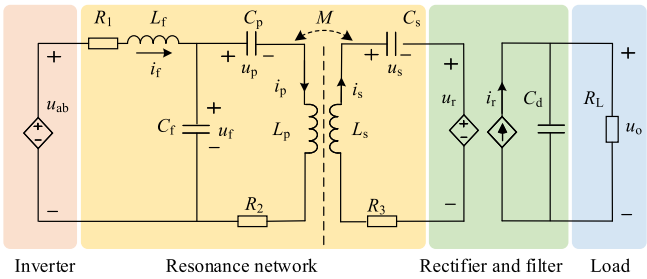

Fig. 4. Equivalent circuit diagram of Fig. 1.

B. Circuit Theory-Based Modeling

A large-signal model of the WPT system can be established according to the simplified circuit as shown in Fig. 4, where u_r and i_r represent the voltage and the current of the rectifier bridge, respectively. According to Fig. 4 and Kirchhoff's theorem, the system can be described by the following:

$$\begin{cases} L_\mathrm{f}\dfrac{\mathrm{d}i_\mathrm{f}}{\mathrm{d}t} + R_1 i_\mathrm{f} + u_\mathrm{cf} = u_\mathrm{ab} \\ C_\mathrm{f}\dfrac{\mathrm{d}u_\mathrm{cf}}{\mathrm{d}t} + i_\mathrm{p} = i_\mathrm{f} \\ C_\mathrm{p}\dfrac{\mathrm{d}u_\mathrm{cp}}{\mathrm{d}t} = i_\mathrm{p} \\ L_\mathrm{p}\dfrac{\mathrm{d}i_\mathrm{p}}{\mathrm{d}t} + R_2 i_\mathrm{p} + u_\mathrm{cp} - M\dfrac{\mathrm{d}i_\mathrm{s}}{\mathrm{d}t} = u_\mathrm{cf} \\ -L_\mathrm{s}\dfrac{\mathrm{d}i_\mathrm{s}}{\mathrm{d}t} - R_3 i_\mathrm{s} - u_\mathrm{cs} + M\dfrac{\mathrm{d}i_\mathrm{p}}{\mathrm{d}t} = u_\mathrm{r} \\ C_\mathrm{s}\dfrac{\mathrm{d}u_\mathrm{cs}}{\mathrm{d}t} = i_\mathrm{s} \\ C_\mathrm{d}\dfrac{\mathrm{d}u_\mathrm{o}}{\mathrm{d}t} + \dfrac{u_\mathrm{o}}{R_\mathrm{L}} = i_\mathrm{r} \end{cases} \tag{1}$$

where u_r and i_r can be calculated based on energy conservation. According to [17] and[32], u_r and i_r can be expressed as follows:

$$\begin{cases} i_\mathrm{r} = \dfrac{2}{\pi}\sqrt{i_\mathrm{s,d}^2 + i_\mathrm{s,q}^2} \\ u_\mathrm{r} = \dfrac{8}{\pi^2}\dfrac{u_\mathrm{o} i_\mathrm{s}}{i_\mathrm{r}} \end{cases} \tag{2}$$

where $i_\mathrm{s,d}$ and $i_\mathrm{s,q}$ represent the real and imaginary parts of i_s, respectively. The GSSA model of system can then be obtained as

$$\begin{cases} \dot{x}(t) = \mathbf{A}x(t) + \mathbf{B}u(t) \\ y(t) = \mathbf{C}x(t) \end{cases} \tag{3}$$

where $x(t)$ represents the generalized state variable vector, which contains the real and imaginary parts of the state variables in (1). $u(t) = u_\mathrm{ab}$ represents the control input that can be obtained by (4). $y(t) = u_\mathrm{o}$ represents the output of the system. $\mathbf{A}$, $\mathbf{B}$, and $\mathbf{C}$ represent the system, input, and output coefficient matrix of the large-signal model, respectively

$$u_\mathrm{ab} = \frac{4U_\mathrm{dc}}{\pi}\sin\left(\frac{\pi d}{2}\right). \tag{4}$$

For the purpose of control system design, linear models are one of the objectives of conventional modeling methods [18], [33], so one can linearize equation (3) at the given set point to obtain a small-signal model that is linear in the variables. By perturbing and linearizing the state-space equation of the system as (5), the small-signal model can be obtained. $\widehat{x}_i$, $\widehat{u}_\mathrm{ab}$, $\widehat{y}$, and γ represent the perturbation performed around the steady-state operating point. $\overline{U}_\mathrm{ab}$, $\overline{U}_\mathrm{o}$, and $\overline{D}$ denote the input voltage, output voltage, and duty cycle at stable operating point, and $\overline{Y} = \overline{U}_\mathrm{o}$

$$\begin{cases} x_i = \overline{X}_i + \widehat{x}_i \\ u_\mathrm{ab} = \overline{U}_\mathrm{ab} + \widehat{u}_\mathrm{ab} \\ y = \overline{Y} + \widehat{y} \\ d = \overline{D} + \widehat{d} \end{cases} \tag{5}$$

where capital letters stand for steady-state values, which can be calculated by setting the derivative in (3) to zero. $\overline{U}_\mathrm{ab}$ and $\widehat{u}_\mathrm{ab}$ can be calculated as

$$\overline{U}_\mathrm{ab} = \frac{4U_\mathrm{dc}}{\pi}\sin\left(\frac{\pi\overline{D}}{2}\right) \tag{6}$$

$$\widehat{u}_\mathrm{ab} = \left.\frac{\partial u_\mathrm{ab}}{\partial d}\right|_{d=\overline{D}}\widehat{d} = 2U_\mathrm{dc}\cos\left(\frac{\pi\overline{D}}{2}\right)\widehat{d}. \tag{7}$$

Therefore, the state-space equation of the small-signal model is established as

$$\begin{cases} \dot{\widehat{x}}(t) = \widehat{\mathbf{A}}\widehat{x}(t) + \widehat{\mathbf{B}}\widehat{u}(t) \\ \widehat{y}(t) = \widehat{\mathbf{C}}\widehat{x}(t) \end{cases} \tag{8}$$

where $\widehat{u}(t) = \widehat{d}$ and $\widehat{y}(t) = \widehat{u}_\mathrm{o}$ represent the input and output variables of the state-space model. $\widehat{\mathbf{A}}$, $\widehat{\mathbf{B}}$, and $\widehat{\mathbf{C}}$ represent the coefficient matrices of the small-signal model. Through (8), a transfer function form of (8) can be derived as

$$\widehat{G}_\mathrm{m}(s) = \frac{\widehat{Y}(s)}{\widehat{U}(s)} = \widehat{\mathbf{C}}(s\mathbf{I} - \widehat{\mathbf{A}})^{-1}\widehat{\mathbf{B}} \tag{9}$$

where $\mathbf{I}$ represents an identity matrix of appropriate dimension, and $\widehat{G}_\mathrm{m}(s)$ denotes the small-signal transfer function. $\widehat{U}(s)$ and $\widehat{Y}(s)$ represent the input and output in the frequency domain. Then, by using the parameters in Table I, a 13th-order transfer model function can be derived. One can apply the balance theory and Hankel singular value truncation method to reduce the model order [17], [35]. The singular value distribution of

TABLE I
MAIN CIRCUIT PARAMETERS

Items	Symbol	Value
DC Input Voltage	U_{dc}	150 V
Operation frequency	f_0	100 kHz
Parallel compensation capacitor	C_{f}	102.54 nF
Primary series compensation capacitor	C_{p}	16.86 nF
Secondary series compensation capacitor	C_{s}	13.42 nF
Filter capacitor	C_{d}	470 μF
Compensation inductance	L_{f}	24.77 μH
Transmitting coil inductance	L_{p}	173.93 μH
Receiver coil inductance	L_{s}	186.47 μH
Mutual inductance	M	37.49 μH
Compensation inductance impedance	R_1	0.02 Ω
Transmitting coil impedance	R_2	0.18 Ω
Receiver coil impedance	R_3	0.19 Ω
Output power range	P_{out}	0$\sim$1.3 kW
Load	R_{L}	64 Ω

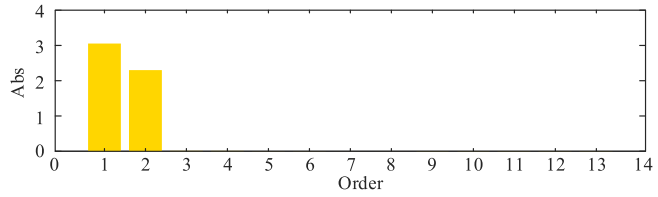

Fig. 5. Singular value distribution of of the full-order model.

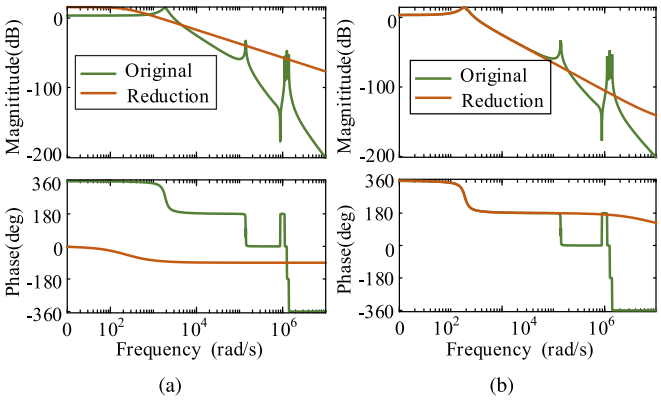

Fig. 6. Bode diagram of reduced-order models. (a) First-order model. (b) Second-order model.

the full-order model is shown in Fig. 5, which indicates that a second-order reduced-order model could be the best. The bode diagrams of the original model and the reduced-order model are shown in Fig. 6. In the frequency range of $[0, 10^5]$ rad/s, the gain and phase curves of the second-order model and the original model almost coincide. Therefore, it is reasonable to use multiple second-order models to approximate the nonlinear behavior of the system, as discussed in [36]. However, this treatment will increase the complexity of the controller. The Hammerstein model, consisting of a static nonlinear function followed by a linear model, can accurately characterize the behavior of the system with input nonlinearity. Through analysis of the large-signal and small-signal models of the WPT system,

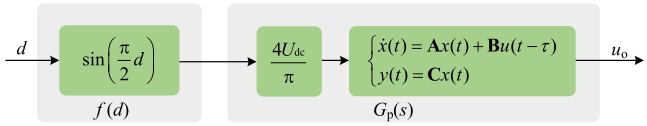

Fig. 7. Block diagram of WPT system based on Hammerstein model.

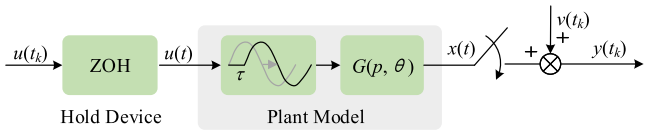

Fig. 8. Block diagram of the linear part of the Hammerstein model.

the Hammerstein model shown in Fig. 7 can be a reasonable alternative to replace the original circuit theory-based model. In the Hammerstein model, $f(d)$ is the static nonlinearity function, d is the duty cycle (control variable), and $G_{\mathrm{p}}(s)$ is a linear time-invariant model. The relationship between u_{o} and d can be simplified as follows:

$$u_{\mathrm{o}} = G_{\mathrm{p}}(s) f(d). \tag{10}$$

Obviously, if we use GSSA to generate the linear model $G_{\mathrm{p}}(s)$, the resulting model will be of very high order, and the model accuracy may not be guaranteed if the component parameters are not accurately known. To avoid this problem, the data-driven modeling method will be used to identify the Hammerstein model in the next section.

C. Data-Driven Modeling

By using the method of data-driven modeling, it is easy to estimate the parameters of the Hammerstein model as shown in Fig. 7. In this article, the static nonlinearity corresponding to a full-bridge inverter is $f(d) = \sin(\pi d/2)$. In addition, this nonlinear function can also be identified from static input–output data (measured after all transients have died out). The dynamic linear model can be identified from the dynamic input and output data, which is related to the transient response generated by an appropriate excitation signal, such as the pseudorandom binary sequence (PRBS). The block diagram of the linear model is shown in Fig. 8, where a time delay is added to account for the communication delay. The Hammerstein model can be written as follows [24]:

$$\begin{cases} x(t) = G(s,\theta) f(u(t-\tau)) = \dfrac{B(s,\theta)}{A(s,\theta)} f(u(t-\tau)) \\ y(t_k) = x(t_k) + v(t_k) \end{cases} \tag{11}$$

in which τ represents the total time delay of the system, $v(t_k)$ represents the output measurement noise, and $t_k = kT$ represents the sampling time (with T the sampling period). $B(s,\theta)$ and $A(s,\theta)$ are the following polynomials:

$$B(s,\theta) = b_0 s^{n_{\mathrm{b}}} + b_1 s^{n_{\mathrm{b}}-1} + \cdots + b_{n_{\mathrm{b}}} \tag{12a}$$

$$A(s,\theta) = s^{n_{\mathrm{a}}} + a_1 s^{n_{\mathrm{a}}-1} + \cdots + a_{n_{\mathrm{a}}} \tag{12b}$$

where $\theta = [a_1, \ldots, a_{n_a}, b_0, \ldots, b_{n_b}]^\top$ is the vector of unknown parameters, with n_a and n_b ($n_a \geqslant n_b$) being polynomial degrees. The previous circuit modeling analysis suggests a second-order model to describe the system behavior, so here, we can set $n_a = 2$ and $n_b = 1$.

Let's make the following assumptions. 1) $B(s, \theta)$ and $A(s, \theta)$ have no common factor. 2) The roots of $A(s, \theta)$ lie in the left-half plane. 3) n_a and n_b are known. 4) $u(t)$ is generated from a discrete sequence $u(t_k)$ via a holding device, which is designed to be independent of other input parameters of the system, and has enough information to ensure the identifiability of the model. The objective of this article is to estimate the vector of parameters θ and the time delay τ, from the sampled input–output data $\{y(t_k), u(t_k)\}_{k=1}^N$, where N is the number of samples.

The following optimization problem is defined to estimate the unknown model parameters:

$$\widehat{\theta}, \widehat{\tau} = \arg\min_{\theta,\tau} J(\theta, \tau) \tag{13}$$

$$J(\theta, \tau) = \arg\min_{\theta,\tau} \frac{1}{2N} \sum_{k=1}^{N} \varepsilon^2(t_k) \tag{14}$$

$$\varepsilon(t_k) = y(t_k) - x(t_k) \tag{15}$$

where $J(\theta, \tau)$ is the cost function and $\varepsilon(t_k)$ is the output error at the kth sampling time. Newton's steepest gradient descent method has the characteristics of fast convergence, so it is used here to iteratively estimate the parameters θ and τ. For convenience in the notations, let us define

$$\rho = \begin{bmatrix} \theta \\ \tau \end{bmatrix} \tag{16}$$

the iterative estimation of ρ is given as

$$\widehat{\rho}^{j+1} = \widehat{\rho}^{j} - \mu^j \left(\nabla^2 J(\rho)\right)^{-1} \nabla J(\rho)\big|_{\rho=\widehat{\rho}^j} \tag{17}$$

where μ is the step length, $\nabla J(\theta)$ and $\nabla^2 J(\rho)$ denote the gradient vector and approximated Hessian matrix, respectively

$$\nabla J(\rho) = \sum_{k=1}^{N} \left(\frac{\partial \varepsilon(t_k)}{\partial \theta}\right)^\top \varepsilon(t_k) \tag{18}$$

$$\nabla^2 J(\rho) = \sum_{k=1}^{N} \left(\frac{\partial \varepsilon(t_k)}{\partial \theta}\right)^\top \left(\frac{\partial \varepsilon(t_k)}{\partial \theta}\right). \tag{19}$$

The proposed algorithm is summarized as Algorithm 1. First, the initial values of parameters are set, such as model parameters, time delay, minimum error increment, etc. Then, the unknown parameters are estimated by Newton's iterative search, and the iterative calculation is repeated until the optimal parameter estimates are obtained.

Algorithm 1: Newton's Iterative Searching Method.

Input:
- Sampled data: $\{y(t_k), u(t_k)\}_{k=1}^N$;
- Polynomial degrees: $\{n_a, n_b\}$;
- Number of training data and iterations: N_0, N_{iter};
- Initial parameters of time delay $\{\tau^0, \Delta\tau_{\min}, \tau_{\max}\}$;
- Tolerances: $\varsigma_{\text{fun}}, \varsigma_{\text{par}}$.

Output: ρ^*;

```
based on τ^0, estimate θ^0 via a linear model estimation method;
ρ* ← [θ^0; τ^0];
for j ← 1 to N_iter do
    μ ← 1;
    compute Δρ* = (∇²J(ρ*))^{-1} ∇J(ρ*);
    implement the following:
    for i ← 1 to N_iter do
        compute ρ̂ = ρ* − μΔρ*;
        if J(ρ̂) ⩾ J(ρ*) or τ̂ ≠ [τ_min, τ_max] then
            μ ← μ/2;
            if ‖μΔρ./ρ̂^j‖ < ς_par then break;
        else
            ρ* ← ρ̂; break;
        end
    end
    if |ΔJ(ρ*)/J(ρ*)| < ς_fun or ‖μΔρ./ρ*‖ < ς_par
     then break;
end
```

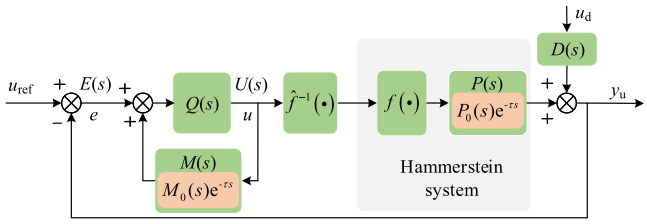

Fig. 9. Block diagram of the IMC scheme based on the Hammerstein model.

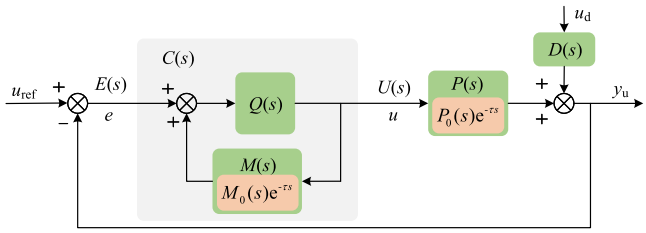

Fig. 10. Block diagram of the equivalent IMC scheme.

III. Control Design

A. Hammerstein-Model-Based IMC Scheme

The Hammerstein-model-based IMC is shown in Fig. 9. When the nonlinear component $f(\cdot)$ of the system is fully compensated for, the control system in Fig. 9 is equivalent to the one shown in Fig. 10, which is the standard internal model control structure. $Q(s)$ denotes the internal model controller. $P(s)$ denotes the WPT system. $M(s)$ denotes the mathematical model of the plant obtained by the data-driven method. e denotes the error between the output voltage y_u and the set voltage u_{ref}. $U(s)$ represents

the output of the feedback controller, and $D(s)$ denotes the disturbance transfer function. $C(s)$ denotes the feedback controller (the shadowed part of Fig. 10). The control objective is to force the output voltage y_{u} to track the set value u_{ref}. The closed-loop transfer function can be written as follows:

$$y_{\mathrm{u}} = \frac{Q(s)P(s)}{1+Q(s)(P(s)-M(s))}u_{\mathrm{ref}} + \frac{(1-Q(s)M(s))D(s)}{1+Q(s)(P(s)-M(s))}u_{\mathrm{d}} \tag{20}$$

and the error is expressed as

$$e = u_{\mathrm{ref}} - y_{\mathrm{u}} = \frac{(1-Q(s)M(s))}{1+Q(s)(P(s)-M(s))}(u_{\mathrm{ref}} - u_{\mathrm{d}}). \tag{21}$$

Remark 1: If the plant $P(s)$ is stable and $P(s) = M(s)$. $Q(s) = M^{-1}(s)$ can be computed. The disturbance $u_{\mathrm{d}} \neq 0$ and the step input $u_{\mathrm{ref}} \neq 0$. According to (20), the system output is maintained equal to the set value as $y_{\mathrm{u}} = u_{\mathrm{ref}}$, and the ideal control performance can be obtained.

Remark 2: The closed-loop system is stable. $Q(0)M(0) = 1$, where $Q(0)$ denotes the steady-state gain of the controller and $M(0)$ denotes the estimated model gain. The disturbance $u_{\mathrm{d}} \neq 0$ and the step input $u_{\mathrm{d}} \neq 0$. According to (21), even if $P(s) \neq M(s)$, $y_{\mathrm{u}} = u_{\mathrm{ref}}$.

Unlike the above ideal situations, the following practical issues need to be considered. 1) Communication delays are inevitable and they will introduce a pure delay in $M^{-1}(s)$, then $M^{-1}(s)$ is physically difficult to realize. 2) If the model contains RHP zeros, the controller $Q(s)$ will have RHP poles and the controller itself will be unstable, which will lead to the instability of the closed-loop system. 3) The model $M(s)$ is strictly rational, but the ideal controller is not rational, i.e., the n-order differentiator will appear in the controller. 4) If the closed-loop system is composed of an ideal controller, the output of the closed-loop system is sensitive to the model error, i.e., $P(s) \neq M(s)$, and then the robustness of the closed-loop system may not be guaranteed.

Therefore, the process model needs to be decomposed: only the part containing stable zeros and stable poles is used to design the controller.

B. IMC Control Design

1) Parameter Design: The IMC controller design has two steps. 1) A stable ideal controller is designed without considering the robustness and constraints of the system. 2) A filter $f(s)$ is introduced, and the desired dynamic robustness is obtained by adjusting the structure and parameters of the filter.

1) The model $M(s)$ is decomposed as follow:

$$M(s) = M_+(s)M_-(s) \tag{22}$$

where $M_+(s)$ contains the time delay and the nonminimum phase part (e.g., RHP zeros), and $M_-(s)$ is the minimum phase part of the model.

2) To ensure the stability and robustness of the closed-loop system, a filter is introduced. The controller is defined as

$$Q(s) = f(s)/M_-(s) \tag{23}$$

$$f(s) = 1/(1+\lambda s)^n \tag{24}$$

where $f(s)$ is a low-pass filter of order n, which ensures that $Q(s)$ is rational. λ is the time constant of the filter, which could balance the tracking performance and robustness of the controller. Since the WPT system can be described by a second-order plus time delay, n can be set to 2. The feedback controller $C(s)$ can be obtained as

$$C(s) = \frac{U(s)}{E(s)} = \frac{Q(s)}{1-Q(s)M(s)} = \frac{M_-^{-1}(s)}{f^{-1}(s)-M_+(s)} \tag{25}$$

and the controller output is

$$U(s) = \frac{M_-^{-1}(s)E(s)}{f^{-1}(s)-M_+(s)}. \tag{26}$$

Remark 3: $M(s)$ and $P(s)$ generally do not match. According to the robustness theorem, the closed-loop stability condition of IMC is

$$|M_+(s)f(s)| \leqslant 1/l_{\mathrm{m}} \quad \forall\omega \tag{27}$$

where l_{m} is the upper bound of model uncertainties

$$E_{\mathrm{m}}(s) = \left|\frac{P(s)-M(s)}{P(s)}\right| \leqslant l_{\mathrm{m}}. \tag{28}$$

Assuming that $|M_+(s)| = 1$, when $E_{\mathrm{m}}(s)$ increases, $|f(s)|$ needs to be selected smaller. Since we have $M_+(0)f(0) = 1$ in IMC, the feedback error e satisfies

$$e \leqslant \frac{|1-M_+(s)f(s)|}{1-|M_+(s)f(s)E_{\mathrm{m}}(s)|}|u_{\mathrm{ref}} - u_{\mathrm{d}}| \tag{29}$$

$$e \leqslant |1-M_+(s)f(s))|\,|r-d| = |s|\,|u_{\mathrm{ref}} - u_{\mathrm{d}}|. \tag{30}$$

When $\omega \leqslant 1/\lambda$, we have $M_+(s)f(s) \approx 1$ and $e = 0$. When $\omega \geqslant 1/\lambda$, then $|f(s)|$ is very small, and $|M_+(s)f(s)E_{\mathrm{m}}(s)| \approx 0$. This means that (29) and (30) could be identical. For both high- and low-frequency dynamics, λ should be large enough to ensure that the closed-loop response is sufficiently close to the response of the nominal $M_+(s)f(s)$.

Assume that the model of the WPT system has been reduced to the following one:

$$M(s) = \frac{K}{s^2+2\xi\omega_0 s+\omega_0^2}\mathrm{e}^{-\tau s} \tag{31}$$

where K represents the open-loop process gain, ω_0 represents the natural frequency of the WPT system, ξ represents the damping coefficient, and τ represent the time delay. $M(s)$ can be decomposed as

$$\begin{cases} M_+(s) = \mathrm{e}^{-\tau s} \\ M_-(s) = \dfrac{K}{s^2+2\xi\omega_0 s+\omega_0^2}. \end{cases} \tag{32}$$

Owing to a large time delay existing in the closed-loop system, the controller output is decomposed as follows:

$$U(s) = \frac{f(s)}{M_-(s)}E(s) + f(s)M_+(s)U(s)$$

$$= U_1(s) + U_2(s). \tag{33}$$

Note that only $U_2(s)$ contains the time delay. The analytical expressions of $U_1(s)$ and $U_2(s)$ are

$$U_1(s) = \frac{f(s)}{M_-(s)}E(s) = \frac{1}{K(1+\lambda s)^2}(s^2 + 2\xi\omega_0 s + \omega_0^2)E(s) \tag{34}$$

$$U_2(s) = f(s)M_+(s)U(s) = \frac{1}{K(1+\lambda s)^2}\mathrm{e}^{-\tau s}U(s). \tag{35}$$

The decomposed $U_1(s)$ and $U_2(s)$ can be computed separately. For digital simulation, they can be expressed in state-space form

$$\begin{cases} \dot{x}_1(t) = \mathbf{A}_1 x_1(t) + \mathbf{B}_1 e(t) \\ y_1(t) = \mathbf{C}_1 x_1(t) + \mathbf{D}_1 e_1(t) \end{cases} \tag{36}$$

and

$$\begin{cases} \dot{x}_2(t) = \mathbf{A}_2 x_2(t) + \mathbf{B}_2 y(t-\tau) \\ y_2(t) = \mathbf{C}_2 x_2(t). \end{cases} \tag{37}$$

The control output is then the sum of the outputs of the above models

$$y(t) = y_1(t) + y_2(t). \tag{38}$$

The state equations in (36)–(38) should be discretized when they are implemented in a digital controller. For (38) where a pure time delay appears, conventional methods usually use Padé approximation or Taylor series expansion to approximate the pure time delay. However, if the time delay is large, the accuracy of approximation could not be guaranteed. At the same time, the order of the series expansion will be very high for large time delays, which is not expected in control system implementation. To avoid this problem, we present a method that is able to explicitly address the fractional time delay in digital simulation in a computationally efficient manner (see Appendix).

2) Choice of λ: Sensitivity quantitatively indicates the sensitivity of the closed-loop transfer function to the change of process parameters. The smaller the sensitivity, the stronger the robustness of the control system to the model mismatch. The maximum sensitivity, denoted by M_s, is a robust performance index of a closed-loop system. λ can be obtained by solving the nonlinear equation between M_s and the open-loop transfer function of the containing controller. M_s is defined as

$$M_\mathrm{s} = \max\left|\frac{1}{1+C(s)P(s)}\right|. \tag{39}$$

By combining (24) with (30), $C(s)$ is derived as follows:

$$C(s) = \frac{U(s)}{E(s)} = \frac{Q(s)}{1-Q(s)M(s)} = \frac{s^2 + 2\xi\omega_0 s + \omega_0^2}{K(\lambda^2 s^2 + 2\lambda s + 1 - \mathrm{e}^{-\tau s})}. \tag{40}$$

If the time delay in the above equation is relatively small, the approximation of $\mathrm{e}^{-\tau s} \approx 1 - \tau s$ could be accurate, and then M_s becomes

$$M_\mathrm{s} = \max_{0\leqslant\omega\leqslant\infty}\left|\frac{\lambda^2(j\omega)^2 + 2\lambda(j\omega) + \tau(j\omega)}{\lambda^2(j\omega)^2 + 2\lambda(j\omega) + 1}\right|. \tag{41}$$

Note that λ is the only adjustable parameter in IMC, and it plays a role in balancing the tracking speed and robustness. M_s as the performance index can help us find an optimal value of λ to achieve the desired control performance and its empirical value meets $M_\mathrm{s} \leqslant 2$. Usually, the λ resulted from the optimization of M_s can only be used as an initial value and, starting from this, λ is subsequently adjusted until the robustness index of the system response is met [29], [30].

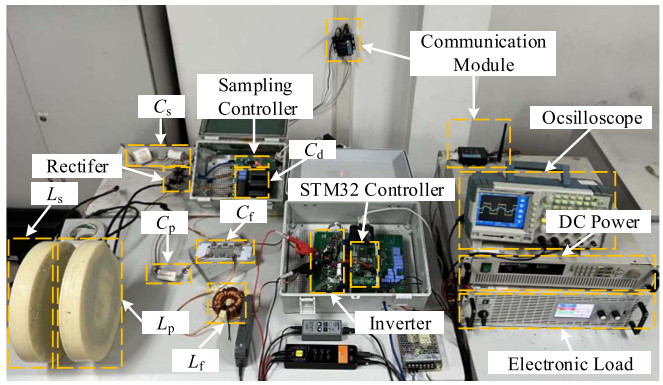

Fig. 11. Experimental setup.

IV. Experimental Results

In this section, experimental results are provided to verify the effectiveness of the proposed modeling and control method. Fig. 11 shows the prototype of the WPT system. On the primary side, a control board with STM32H7 is adopted to realize the IMC control, the signal processing, and the communication function. On the secondary side, STM32F407 is used to realize the sampling and communication functions. The main parameters of the system are shown in Table I. The experimental results of the model parameter estimation and IMC control are illustrated as follows.

A. Validation of Data-Driven Modeling

To show the static input nonlinearity of the system, the steady-state input and output data at multiple static operation points are acquired. The steady-stage outputs as a function of the duty cycle are plotted in Fig. 12(a), where an obvious nonlinearity close to $225 \cdot \sin(\pi d/2)$ can be observed. The steady-state operating points $(\mathrm{m}_1, \mathrm{m}_2, \mathrm{m}_3, \mathrm{m}_4)$ shown in Fig. 12(a) are superimposed with a 2% duty cycle disturbance, and the dynamic responses to these disturbances (with static values removed) are shown in Fig. 12(b). Clearly, all the dynamic responses have the same trend of variation, but the gains differ from each other. This concretes the static nonlinear characteristics of the system. In Fig. 12(b), a disturbance with a very small change in duty cycle (2%) was superimposed to perturb the system. The resulted load voltage variation is small compared with the static output

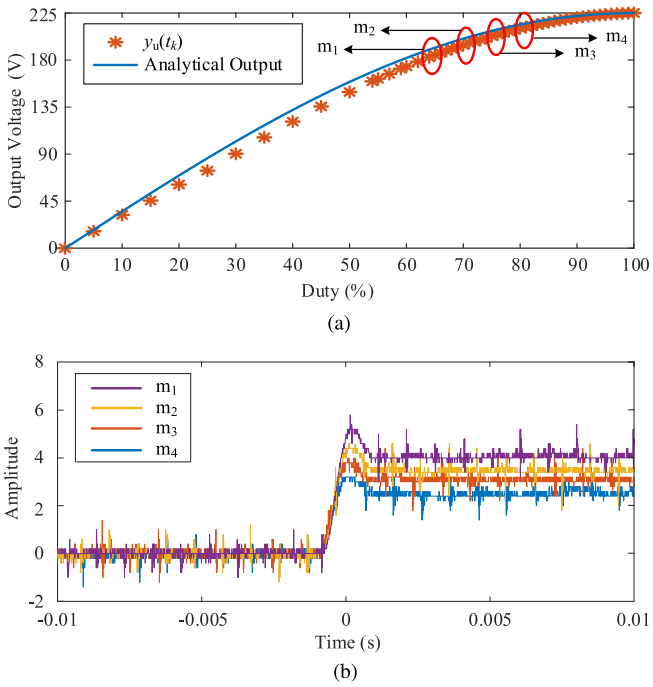

Fig. 12. Static nonlinearity. (a) Static outputs as a function of duty cycle. (b) Step responses to a 2% increment in duty cycle at different static points.

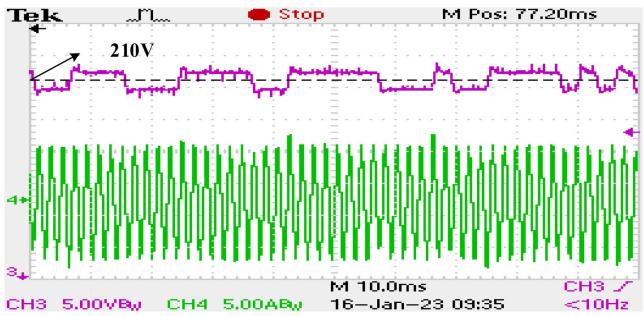

Fig. 13. Portion of the perturbed output voltage and inverter current.

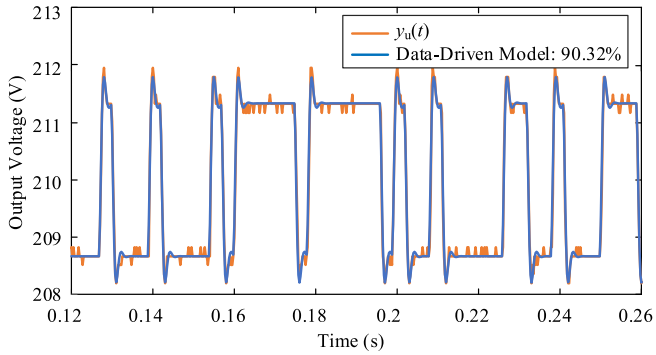

Fig. 14. Comparison of the measured output and estimated model output.

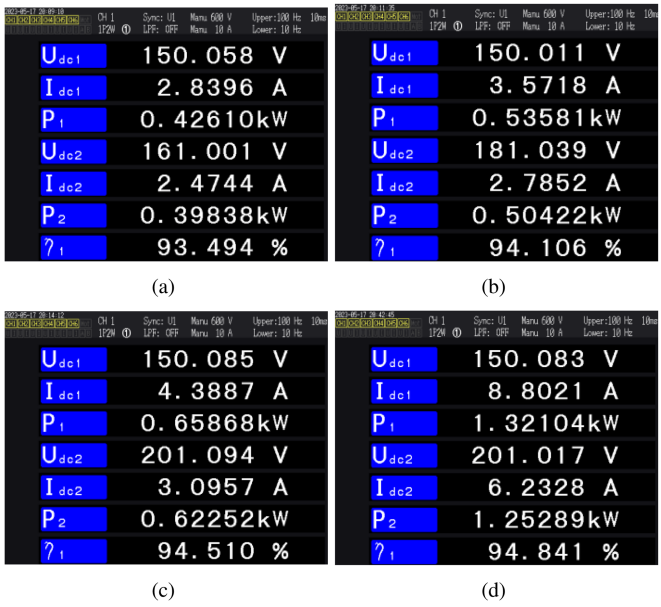

Fig. 15. Input and output of system under different set voltage and load. (a) $u_{\text{ref}} = 161$ V and $R_{\text{L}} = 64\ \Omega$. (b) $u_{\text{ref}} = 181$ V and $R_{\text{L}} = 64\ \Omega$. (c) $u_{\text{ref}} = 201$ V and $R_{\text{L}} = 64\ \Omega$. (d) $u_{\text{ref}} = 201$ V and $R_{\text{L}} = 32\ \Omega$.

(4 versus 200 V), or with the switching noise introduced by the MOSFETs. So, the "zooming" effect of Fig. 12(b) makes switching noise spikes are quite significant. However, if we increase the amplitude of the excitation signal, then these spikes will not be so obvious. It should be mentioned that the difference between the experimental and theoretical (i.e., $225 \cdot \sin(\pi d/2)$) results shown in Fig. 12(a) is attributed to the omission of higher harmonic components. To accurately describe the input nonlinearity, the lookup table (LUT) method is a good option.

The data for rational parameter estimation of the Hammerstein model are generated at the steady-state operating point of $\overline{D} = 0.8$. The steady-state output at this operating point is measured to be 210 V. After that, a PRBS input with an amplitude of 1% duty cycle is superimposed on the steady-state input and, subsequently, a total of 3300 input–output data are sampled. The dynamic output response of the system to the PRBS input excitation is shown in Fig. 13. The average output is 209.92 V, and the amplitude of perturbation on the output is about 5 V. The small perturbation will not affect the running of the system too much.

TABLE II
ESTIMATED PARAMETERS AT STEADY-STATE OPERATION POINTS

Order	Estimated parameter values				fit (%)
	$\widehat{a}_1$	$\widehat{a}_2$	$\widehat{b}_0$	$\widehat{\tau}$(s)	
1	$1.037 \cdot 10^6$		$4.438 \cdot 10^3$	$4.8 \cdot 10^{-3}$	83.31
2	$1.936 \cdot 10^9$	$2.849 \cdot 10^3$	$8.49 \cdot 10^6$	$4.9 \cdot 10^{-3}$	90.32

A comparison between the measured output and the estimated second-order model output is shown in Fig. 14.

The ratio of fitness, computed via the `compare` routine in the control system toolbox in MATLAB, reaches 90.32%, which concretes the accuracy of the data-driven modeling method. The estimated model parameters are shown in Table II, where the second-order model achieves a higher fitness ratio than the first-order model. This illustrates that the second-order model is more

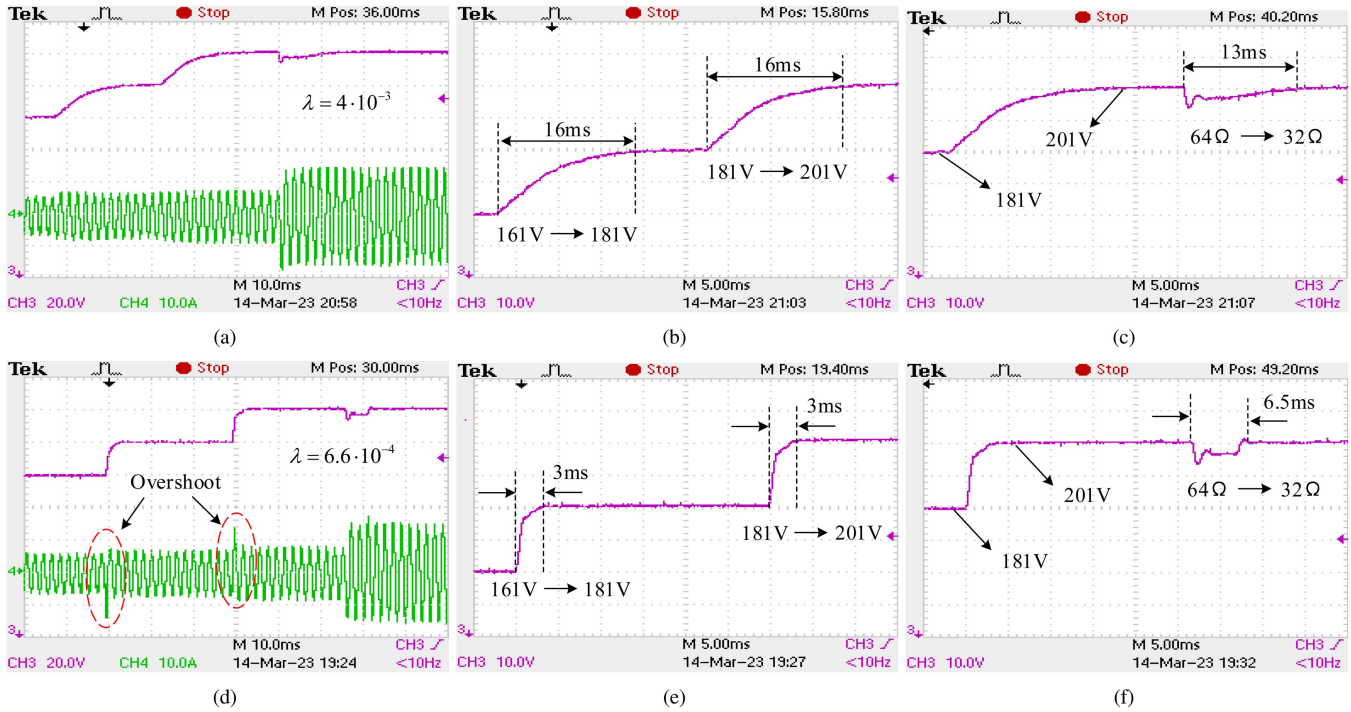

Fig. 16. Experimental results for IMC with different values of λ. (a)–(d) Output voltage of closed-loop system and output current of the inverter. (b)–(e) Dynamic response of reference change. (c)–(f) Dynamic response to load variation.

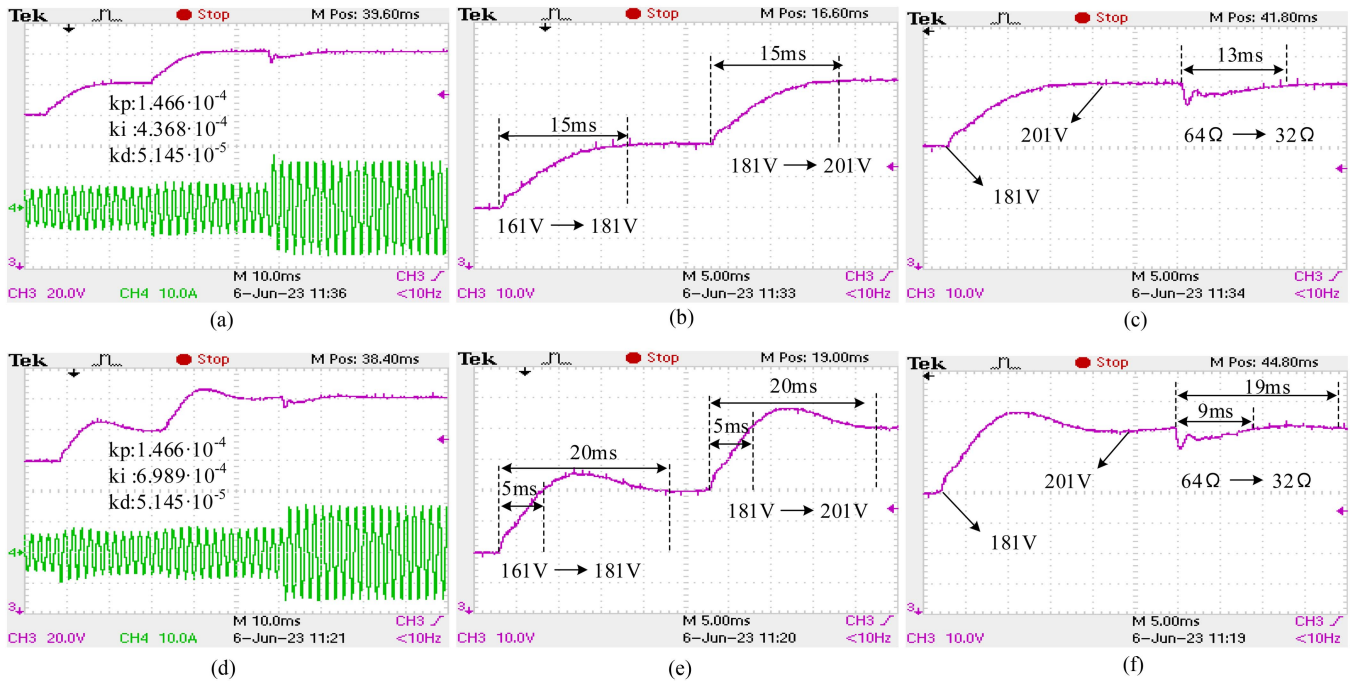

Fig. 17. Experimental results for PID control with different integral gain values of k_i. (a)–(d) Output voltage of closed-loop system and output current of the inverter. (b)–(e) Dynamic response to reference change. (c)–(f) Dynamic response to load variation.

accurate than the first-order model for the WPT system under consideration. Besides, the time delay (measured approximately as $4.9 \cdot 10^{-3}$ s in experiment) has been estimated as $4.8 \cdot 10^{-3}$ s (first-order model) and $4.9 \cdot 10^{-3}$ s (second-order model) through the proposed identification method. The estimated time delay is inconsistent, which is caused by the different phases between the first- and second-order models.

B. Validation of Hammerstein-Model-Based IMC Scheme

To verify the good performance of the proposed Hammerstein-model-based IMC controller, transient response tests and load variation tests have been carried out. All the tests have the same trajectory: they consist of two set point changes, i.e., $u_{\mathrm{ref}} = 161 \rightarrow 181$ V and $u_{\mathrm{ref}} = 181 \rightarrow 201$ V, and one load change, i.e., $R_{\mathrm{L}} = 64 \rightarrow 32\ \Omega$. The control period is 1 ms. The set point and load are changed after the system output reaches a steady state. The power transfer efficiency is measured by a power analyzer (HIOKI PW6001). The steady-state values of input power and output power are shown in Fig. 15. U_{dc1}, I_{dc1}, and P_{dc1} represent, respectively, input voltage, input current, and input power on the dc power supply input side. U_{dc2}, I_{dc2}, and P_{dc2} represent, respectively, output voltage, output current, and output power on the rectifier side of the WPT system. Fig. 15(a)–(c) shows the test results under different set voltages u_{ref}, and 15(d) shows the test result under load changing with $u_{\mathrm{ref}} = 201$ V. Throughout the entire testing process, the trend of output power variation is $P_{\mathrm{out}} = 0.398 \rightarrow 0.504 \rightarrow 0.623 \rightarrow 1.253$ kW within the rated output power of 1.3 kW and the power transfer efficiencies η_1 have maintained above 93%. The performance of the Hammerstein-model-based IMC control is shown in Fig. 16, where two values for λ have been tried, i.e., $\lambda = 6.6 \cdot 10^{-4}$ and $\lambda = 4 \cdot 10^{-3}$. Note, based on the abovementioned method, when the sensitivity $M_{\mathrm{s}} = 2$, λ is calculated as $6.77 \cdot 10^{-4}$. After adjustment, λ is set to $6.6 \cdot 10^{-4}$. Similarly, when $M_{\mathrm{s}} = 1$, $\lambda = 4 \cdot 10^{-3}$. As a comparison, the results of PID control are also presented; see Fig. 17, where k_{p}, k_{i} represent the proportional gain and integral gain of the PID controller, respectively. The static nonlinear gain part of the PID controller in the experiment has been optimized and compensated through the LUT method [21], [37]. The parameter design method of PID is introduced in [38] and [39], and the time delay is considered. In both experiments, the CH3 of the oscilloscope records the wave form of the output voltage, while CH4 records the waveform of the inverter current.

Figs. 16(b) and (e), and 17(b) and (e) are, respectively, the zooming parts of the transient output responses shown in Figs. 16(a) and (d), and 17(a) and (d). These waveforms demonstrate that the control system is able to track the set point at different steady-state operating points. The IMC scheme with $\lambda = 6.6 \cdot 10^{-4}$ achieves the best performance, i.e., it achieves the dynamic characteristics of rapid response at different working points, where the settling time is only 3 ms, while this value increases to 16 ms when $\lambda = 4 \cdot 10^{-3}$ is used. This shows the efficacy of λ in balancing the transient performance and robustness. By contrast, the settling time of the PID controller with the integral gain $k_{\mathrm{i}} = 4.368 \cdot 10^{-4}$ is about 15 ms, which is much slower than the IMC controller (with a settling time of 3 ms) of $\lambda = 6.6 \cdot 10^{-4}$, because the IMC controller is designed based on the identified model, which contains enough knowledge about the system dynamics, and that the communication delay has been compensated correctly. Fig. 17(b) and (e) shows that after the integral gain of the PID controller is enhanced, the response speed of the closed-loop system output increases, but significant excessive overshoots of system output voltage and larger settling time. On the other hand, the waveforms of the inverter current in Figs. 16(a) and (d), and 17(a) reveal that fast transient response can lead to overshoots of the inverter current. Therefore, λ should also be carefully chosen in order to avoid inverter damage.

Figs. 16(c) and (f), and 17(c) and (f) show the output responses after the load has been switched from 64 Ω to 32 Ω. In all the tests, the output voltage drops by approximately 6 V, while the recovery times for the four control tests are, respectively, 13, 6.5, 13, and 19 ms. These indicate that the IMC controller of $\lambda = 6.6 \cdot 10^{-4}$ can quickly come back to the steady-state under external disturbances through optimizing λ. Fig. 17(c) and (f) shows that increasing the integral gain of the PID controller to accelerate response speed may lead to overshoots of the system output voltage and more recovery time.

In addition, it is worth mentioning that the proposed method can be applied to WPT systems with other compensation type besides the *LCC*-S topology. The proposed method is a universal approach to identify the Hammerstein model of the WPT system and design an IMC controller based on the Hammerstein model. The models of WPT systems with various compensations can be estimated by the proposed identification method in the same way. WPT systems with different compensations are mainly reflected in the model order and parameters, and these differences will not affect the controller design process of the proposed method.

V. Conclusion

This article has considered the problem of identification and control for the *LCC*-S WPT system. To address the high-order, nonlinear characteristics of the system under consideration, as well as the problem of large communication time delays, a Hammerstein model is used and identified to describe the system dynamics and a Hammerstein-model-based IMC controller is designed for delay compensation control. The research outcomes show that a Hammerstein model is a kind of global model that can describe the WPT system in a wider range of operation, and that the data-driven scheme for model identification results in an accurate model of relatively low order. This solves the problems of conventional circuit-theory-based modeling approaches where the resulting models always have a high order and they are not able to estimate time delays. Compared with the traditional PID controller, the proposed IMC controller can achieve faster tracking performance and robustness, and one can conveniently tradeoff between the tracking performance and robustness via a single tuning parameter λ. In addition, we have presented a model simulation method that is able to handle fractional time delays. Simulation and experimental results have verified the good performance of the proposed data-driven modeling and internal model control method.

APPENDIX

Consider the following state-space model:

$$\dot{x}(t_k) = \mathbf{A}x(t_k) + \mathbf{B}u(t_k). \tag{42}$$

Given the initial state $x(t_0) = x_0$, the prediction of $x(t_{k+1})$ can be calculated by the RK4 algorithm as (42)

$$\begin{aligned} x(t_{k+1}) &= x(t_k) + (K_1 + 2K_2 + 2K_3 + K_4)h/6 \\ K_1 &= \mathbf{A}x(t_k) + \mathbf{B}u(t_k) \\ K_2 &= \mathbf{A}(x(t_k) + K_1\, h/2) + \mathbf{B}u(t_k + h/2) \\ K_3 &= \mathbf{A}(x(t_k) + K_2\, h/2) + \mathbf{B}u(t_k + h/2) \\ K_4 &= \mathbf{A}(x(t_k) + K_3\, h) + \mathbf{B}u(t_k + h) \end{aligned} \tag{43}$$

where $K_n, n = 1, \ldots, 4$, are the average slope and h is the simulation interval. In the case of a fractional time delay, we can dynamically change the value of h to ensure the fractional time delay to be correctly handled.

REFERENCES

[1] Y. Zhang, K. Chen, F. He, Z. Zhao, T. Lu, and L. Yuan, "Closed-form oriented modeling and analysis of wireless power transfer system with constant-voltage source and load," *IEEE Trans. Power Electron.*, vol. 31, no. 5, pp. 3472–3481, May 2016.

[2] Y. Fan, Y. Sun, X. Dai, Z. Zuo, and A. You, "Simultaneous wireless power transfer and full-duplex communication with a single coupling interface," *IEEE Trans. Power Electron.*, vol. 36, no. 6, pp. 6313–6322, Jun. 2021.

[3] Z. Liu, Y.-G. Su, Y.-M. Zhao, A. P. Hu, and X. Dai, "Capacitive power transfer system with double t-type resonant network for mobile devices charging/supply," *IEEE Trans. Power Electron.*, vol. 37, no. 2, pp. 2394–2403, Feb. 2022.

[4] Y. Wu, C. Liu, M. Zhou, X. Mao, and Y. Zhang, "An antioffset electric vehicle wireless charging system based on dual coupled antiparallel coils," *IEEE Trans. Power Electron.*, vol. 38, no. 5, pp. 5634–5637, May 2023.

[5] K. Song et al., "A rotation-lightweight wireless power transfer system for solar wing driving," *IEEE Trans. Power Electron.*, vol. 34, no. 9, pp. 8816–8830, Sep. 2019.

[6] J. Qu, L. He, N. Tang, and C.-K. Lee, "Wireless power transfer using domino-resonator for 110-kv power grid online monitoring equipment," *IEEE Trans. Power Electron.*, vol. 35, no. 11, pp. 11380–11390, Nov. 2020.

[7] S. Roy, A. N. M. W. Azad, S. Baidya, M. K. Alam, and F. Khan, "Powering solutions for biomedical sensors and implants inside the human body: A comprehensive review on energy harvesting units, energy storage, and wireless power transfer techniques," *IEEE Trans. Power Electron.*, vol. 37, no. 10, pp. 12237–12263, Oct. 2022.

[8] Z. Yan et al., "Frequency optimization of a loosely coupled underwater wireless power transfer system considering eddy current loss," *IEEE Trans. Ind. Electron.*, vol. 66, no. 5, pp. 3468–3476, May 2019.

[9] Z. Yan, B. Song, Y. Zhang, K. Zhang, Z. Mao, and Y. Hu, "A rotation-free wireless power transfer system with stable output power and efficiency for autonomous underwater vehicles," *IEEE Trans. Power Electron.*, vol. 34, no. 5, pp. 4005–4008, May 2019.

[10] J. Zhou, B. Zhang, W. Xiao, D. Qiu, and Y. Chen, "Nonlinear parity-time-symmetric model for constant efficiency wireless power transfer: Application to a drone-in-flight wireless charging platform," *IEEE Trans. Ind. Electron.*, vol. 66, no. 5, pp. 4097–4107, May 2019.

[11] Y. Geng, Z. Yang, and F. Lin, "Design and control for catenary charged light rail vehicle based on wireless power transfer and hybrid energy storage system," *IEEE Trans. Power Electron.*, vol. 35, no. 8, pp. 7894–7903, Aug. 2020.

[12] E. Abramov and M. M. Peretz, "Adaptive self-tuned controller IC for resonant-based wireless power transfer transmitters," *IEEE Trans. Power Electron.*, vol. 36, no. 11, pp. 12413–12431, Nov. 2021.

[13] S. R. Sanders, J. M. Noworolski, X. Z. Liu, and G. C. Verghese, "Generalized averaging method for power conversion circuits," in *Proc. 21st Annu. IEEE Conf. Power Electron. Specialists*, 1990, pp. 333–340.

[14] A. Forsyth, G. Ward, and S. Mollov, "Extended fundamental frequency analysis of the LCC resonant converter," *IEEE Trans. Power Electron.*, vol. 18, no. 6, pp. 1286–1292, Jun. 2003.

[15] C. S. Tang, Y. Sun, Y. G. Su, S. K. Nguang, and A. P. Hu, "Determining multiple steady-state ZCS operating points of a switch-mode contactless power transfer system," *IEEE Trans. Power Electron.*, vol. 24, no. 2, pp. 416–425, Feb. 2009.

[16] C.-S. Wang, G. Covic, and O. Stielau, "Investigating an LCL load resonant inverter for inductive power transfer applications," *IEEE Trans. Power Electron.*, vol. 19, no. 4, pp. 995–1002, Apr. 2004.

[17] H. Feng and S. M. Lukic, "Reduced-order modeling and design of single-stage LCL compensated IPT system for low voltage vehicle charging applications," *IEEE Trans. Veh. Technol.*, vol. 69, no. 4, pp. 3728–3739, Apr. 2020.

[18] Z. Liu, L. Wang, Y. Guo, and S. Li, "Primary-side linear control for constant current/voltage charging of the wireless power transfer system based on the LCC-N compensation topology," *IEEE Trans. Ind. Electron.*, vol. 69, no. 9, pp. 8895–8904, Sep. 2022.

[19] A. Balestrino, A. Landi, M. Ould-Zmirli, and L. Sani, "Automatic nonlinear auto-tuning method for Hammerstein modeling of electrical drives," *IEEE Trans. Ind. Electron.*, vol. 48, no. 3, pp. 645–655, Jun. 2001.

[20] J.-T. Hsu and K. Ngo, "Behavioral modeling of the IGBT using the Hammerstein configuration," *IEEE Trans. Power Electron.*, vol. 11, no. 6, pp. 746–754, Nov. 1996.

[21] F. Alonge, F. D'Ippolito, F. M. Raimondi, and S. Tumminaro, "Nonlinear modeling of DC/DC converters using the Hammerstein's approach," *IEEE Trans. Power Electron.*, vol. 22, no. 4, pp. 1210–1221, Jul. 2007.

[22] L. Aguirre, P. Donoso-Garcia, and R. Santos-Filho, "Use of a priori information in the identification of global nonlinear models-a case study using a buck converter," *IEEE Trans. Circuits Syst. I: Fundam. Theory Appl.*, vol. 47, no. 7, pp. 1081–1085, Jul. 2000.

[23] F. Chen, P. C. Young, H. Garnier, Q. Deng, and M. K. Kazimierczuk, "Data-driven modeling of wireless power transfer systems with multiple transmitters," *IEEE Trans. Power Electron.*, vol. 35, no. 11, pp. 11363–11379, Nov. 2020.

[24] F. Chen, A. Padilla, P. C. Young, and H. Garnier, "Data-driven modeling of wireless power transfer systems with slowly time-varying parameters," *IEEE Trans. Power Electron.*, vol. 35, no. 11, pp. 12442–12456, Nov. 2020.

[25] M. Al-Greer, M. Armstrong, M. Ahmeid, and D. Giaouris, "Advances on system identification techniques for DC–DC switch mode power converter applications," *IEEE Trans. Power Electron.*, vol. 34, no. 7, pp. 6973–6990, Jul. 2019.

[26] M. Ahmeid, M. Armstrong, S. Gadoue, M. Al-Greer, and P. Missailidis, "Real-time parameter estimation of DC–DC converters using a self-tuned Kalman filter," *IEEE Trans. Power Electron.*, vol. 32, no. 7, pp. 5666–5674, Jul. 2017.

[27] S. Liu et al., "Dynamic improvement of inductive power transfer systems with maximum energy efficiency tracking using model predictive control: Analysis and experimental verification," *IEEE Trans. Power Electron.*, vol. 35, no. 12, pp. 12752–12764, Dec. 2020.

[28] J. Liu, Z. Liu, and H. Su, "Passivity-based PI control for receiver side of dynamic wireless charging system in electric vehicles," *IEEE Trans. Ind. Electron.*, vol. 69, no. 1, pp. 783–794, Jan. 2022.

[29] M. Shamsuzzoha and M. Lee, "IMC- PID controller design for improved disturbance rejection of time-delayed processes," *Ind. Eng. Chem. Res.*, vol. 46, no. 7, pp. 2077–2091, 2007.

[30] T. N. L. Vu, L. H. Giang, L. Linh, and V. L. Chuong, "Advanced IMC-PID controller design for the disturbance rejection of first order plus time delay processes," in *Proc. Int. Conf. Syst. Sci. Eng.*, 2017, pp. 279–283.

[31] M. Shamsuzzoha and M. Lee, "An enhanced performance PID filter controller for first order time delay processes," *J. Chem. Eng. Jpn.*, vol. 40, no. 6, pp. 501–510, 2007.

[32] F. Chen, Z. Deng, H. Hu, and Y. Sun, "Dynamic reduced-order modeling of wireless power transfer systems via polynomial approximation," *IEEE Trans. Power Electron.*, vol. 37, no. 7, pp. 7540–7547, Jul. 2022.

[33] S. Samanta and A. K. Rathore, "Small-signal modeling and closed-loop control of a parallel–series/series resonant converter for wireless inductive power transfer," *IEEE Trans. Ind. Electron.*, vol. 66, no. 1, pp. 172–182, Jan. 2019.

[34] R. Haber and L. Keviczky, "Nonlinear system identification-input-output modeling approach volume 1: Nonlinear system parameter identification," *Math. Modelling Theory Appl.*, vol. 7, pp. 43–49, 1999.

[35] E. R. Samuel, L. Knockaert, and T. Dhaene, "Model order reduction of time-delay systems using a Laguerre expansion technique," *IEEE Trans. Circuits Syst. I: Regular Papers*, vol. 61, no. 6, pp. 1815–1823, Jun. 2014.

[36] D. Q. Dang, Y. Wang, and W. Cai, "Offset-free predictive control for variable speed wind turbines," *IEEE Trans. Sustain. Energy*, vol. 4, no. 1, pp. 2–10, Jan. 2013.
[37] E. D. Sumer, Y. Wang, M. Farid, and D. P. Filev, "Adaptive control of an uncertain Hammerstein actuator model in a variable cam timing system," in *Proc. IEEE Int. Conf. Syst., Man, Cybern.*, 2017, pp. 2261–2266.
[38] S. Srivastava and V. Pandit, "A PI/PID controller for time delay systems with desired closed loop time response and guaranteed gain and phase margins," *J. Process Control*, vol. 37, pp. 70–77, 2016.
[39] Q. Deng, Z. Li, J. Liu, S. Li, P. Luo, and K. Cui, "Data-driven modeling and control considering time delays for WPT system," *IEEE Trans. Power Electron.*, vol. 37, no. 8, pp. 9923–9932, Aug. 2022.

Shijun Zhao was born in Sichuan, China. He received the B.Eng. degree in automation from the Faculty of Information Engineering and Automation, Kunming University of Science and Technology, Yunnan, China, in 2017. He is currently working toward the Ph.D. degree in control theory and control engineering with Chongqing University, Chongqing, China.

His current research interests include modeling, system identification, and control methods of wireless power transfer and power electronics.

Chunsen Tang (Member, IEEE) received the B.S. degree in automation and Ph.D. degree in control theory and control engineering from the College of Automation, Chongqing University, Chongqing, China, in 2004 and 2009, respectively.

In 2008, he was a Research Fellow with the Department of Electrical and Computer Engineering, The University of Auckland, Auckland, New Zealand. In 2009, he was with the College of Automation, Chongqing University, where he is currently a Professor. His current research interests include nonlinear modeling and analysis, intelligent control, and wireless power transfer.

Fengwei Chen was born in Chongqing, China. He received the B.Eng. degree in automation and the M.Eng. degree in control theory and control engineering from Wuhan University, Wuhan, China, in 2009 and 2011, respectively, and the Ph.D. degree in automatic control from the Université de Lorraine, Nancy, France, in 2014.

From 2015 to 2016, he was a Lecturer with the Dalian University of Technology, Dalian, China. From 2017 to 2020, he was an Associate Researcher with Wuhan University. Since 2021, he has been with Chongqing University, Chongqing, China, where he is currently an Associate Professor. His research interests include system identification and parameter estimation, with applications to wireless power transfer.

Dan Zhao was born in Chongqing, China. She received the B.Eng. degree in automation in 2021 from Chongqing University, Chongqing, China, where she is currently working toward the graduate degree with the School of Automation.

Her research interests include system identification and parameter estimation combined with the study of wireless power transfer.

Pengqi Deng received the B.E. degree in automation in 2015 from the College of Automation, Chongqing University, Chongqing, China, where he is currently working toward the Ph.D. degree in the control theory and control engineering.

His research interests include modeling and control optimization of the wireless power transfer.

Jing Xiao was born in 1988. He received the M.Eng. degree in electrical engineering from Beijing Jiaotong University, Beijing, China, in 2013.

His current research interest includes the application areas of wireless power transmission technology.